Fire Safety Journal 159 (2026) 104574

Contents lists available at ScienceDirect

Fire Safety Journal

journal homepage: www.elsevier.com/locate/firesaf

Experimental investigation of cellular steel beams at ambient and elevated temperatures

Luana V. da Silva [a,c,*], Nickolas Giacomitti [b], Débora Ferreira [a], Nuno Lopes [c], Luís M.R. Mesquita [a]

[a] GICoS, Instituto Politécnico de Bragança, Campus Santa Apolónia, 5300-253, Bragança, Portugal
[b] Instituto Politécnico de Bragança, Campus Santa Apolónia, 5300-253, Bragança, Portugal
[c] CERIS, Department of Civil Engineering, University of Aveiro, Campus Universitário de Santiago, 3810-193, Aveiro, Portugal

ARTICLE INFO

Keywords:
Cellular steel beams
Elevated temperature
Experimental test
Fire
Web-post buckling
Vierendeel mechanism

ABSTRACT

Cellular steel beams, commonly used in modern construction, exhibit complex failure mechanisms that have not been thoroughly explored, especially under fire conditions. This research investigates the structural behaviour of cellular beams under both ambient and elevated temperatures, with a focus on load-bearing capacity and failure modes. Experimental tests were conducted on a solid beam and six cellular beams with varying hole spacings and diameters at different temperatures. All beams were tested under three-point bending, subjecting the openings and the web posts to different combinations of bending moments and shear forces. Experimental maximum loads and failure modes are compared with the design method of EN1993-1-13 and EN1993-1-2. At ambient temperature, failure modes varied with beam design: specimens with smaller opening spacings failed by web-post buckling, while larger openings resulted in a Vierendeel mechanism. While the Eurocode predictions for load capacity were conservative under ambient conditions, the design model did not accurately predict the correct failure mode. Elevated temperatures significantly reduced the load capacity and, in some cases, changed the collapse mechanism. These results highlight that current design rules are unreliable in predicting the failure mode and may not ensure safety at higher temperatures, stressing the need for specific design rules for cellular beams in fire conditions.

1. Introduction

Steel beams with large web openings have become increasingly prominent in civil construction due to their dual functionality: enabling long spans while providing space for essential services such as ventilation systems, pipework, and electrical installations [1,2]. These beams are typically manufactured by making two cutting passes through a solid parent beam, followed by welding the two Tees sections, which increases the beam's depth, improves material efficiency, and enhances load-carrying capacity. Among various web opening geometries, such as hexagonal, sinusoidal, and rectangular, cellular beams with circular openings are particularly preferred for their structural efficiency and ease of fabrication.

Despite their advantages, cellular beams exhibit complex structural behaviour due to the interaction between geometry and failure mechanisms. The introduction of web openings influences the pre-existing failure modes observed in solid beams, such as lateral-torsional buckling [3,4], and gives rise to new ones. A commonly observed local failure mode is the web-post buckling (WPB), wherein the web-post develops an S-shaped double curvature caused by horizontal shear stresses in this region [5]. The resistance to WPB is primarily influenced by the web thickness, the width of the web-post, and the opening height [6–8].

Another critical failure mode is the Vierendeel mechanism (VM), which occurs due to the transfer of vertical shear in the web openings. This transfer induces secondary bending moments, known as Vierendeel bending moments, ensuring equilibrium due to the changes of bending moment along the beam [1,9]. The interaction between these secondary moments, with the global bending moment and the shear load results in the four plastic hinges, two in the top Tee and two in the bottom Tee, around the web openings, particularly in regions with high shear [1,10]. These plastic hinges significantly reduce the beam's load-carrying capacity and lead to increased local deflections [11].

Under fire conditions, the performance of cellular beams becomes

* Corresponding author. GICoS, Instituto Politécnico de Bragança, Campus Santa Apolónia, 5300-253, Bragança, Portugal.
E-mail address: luana.silva@ipb.pt (L.V. da Silva).

https://doi.org/10.1016/j.firesaf.2025.104574
Received 16 January 2025; Received in revised form 30 September 2025; Accepted 2 November 2025
Available online 3 November 2025

critically important due to the adverse effects of elevated temperatures on steel properties. High temperatures significantly reduce the material's strength and stiffness, thereby altering the load-bearing capacity and failure mechanisms of these beams. According to Ref. [12], web-post buckling by shear tends to be one of the most critical failure modes in fire scenarios, especially in beams with slender webs. As the temperature increases, the elasticity modulus of steel decreases faster than its strength, making the beam more prone to instability and failure. While the recently updated EN 1993-1-13:2024 [13] offers guidance for the design of beams with large web openings under ambient conditions, it does not address their structural behaviour in fire scenarios. Similarly, although the updated EN 1993-1-2:2024 [14] includes Annex E, which specifically applies to beams with large web openings, its recommendations are limited to thermal and mechanical responses. For mechanical response, it suggests applying reduction factors to account for the reduction in yield strength and the modulus of elasticity at elevated temperatures.

Although cellular beams in fire conditions have been investigated numerically [4,15,16], experimental investigations are crucial for bridging the knowledge gap in the behaviour of cellular beams under fire conditions. While numerical models provide valuable predictions, they rely on assumptions and simplifications that cannot fully capture the complex, varying interactions occurring in real fire scenarios. Experimental tests allow for direct observation of actual beam behaviour under controlled conditions, providing data that can validate, refine, and enhance these models. While previous studies have predominantly focused on the performance of cellular beams at ambient temperature [5,17–23] research on their performance at elevated temperatures remains limited. Some studies have explored the influence of intumescent paints [24,25] and others analysed full-scale structures, including slabs [26–29] and modular systems [30], in fire scenarios with constant load. However, there is a significant need for experimental investigations on cellular beams without additional components such as slabs or composite sections, tested under steady-state conditions. These tests are particularly valuable because they isolate the effects of constant temperature on beam performance, enabling a more precise understanding of how the material properties, failure modes and load-bearing capacity changes at different temperatures.

This research aims to address the behaviour of cellular beams under fire conditions by providing detailed experimental data. Despite ongoing advancements in fire safety regulations and design guidelines for structural elements, comprehensive experimental investigations on cellular beams in fire scenarios remain scarce. This study will contribute valuable data on the performance of cellular beams subjected to steady-state temperature conditions, offering insights into failure modes, load-bearing capacity, and temperature-dependent behaviour. The findings provide a more comprehensive background for new design rules, ultimately enhancing the fire resistance and safety of structures that incorporate cellular beams.

2. Eurocode verification for cellular beams

The design of steel structures is primarily governed by EN 1993-1-1 [31], establishing general rules and principles for designing steel components. As part of the Eurocode 3 framework, the recent EN 1993-1-13 [13] specifically addresses the design of beams with large web openings. It requires that these beams must be verified both at the location of the openings and in the surrounding regions, ensuring that the structure complies with the safety and performance requirements at the ultimate limit state. The main geometric parameters defining the cellular beams, including the cross-section dimensions, are shown in Fig. 1(a).

In accordance with the Eurocodes, the design verification for bending resistance requires that the design value of the bending moment, M_{Ed}, does not exceed the design bending resistance of the cross-section. This verification is carried out for both the solid I-section of the beam, where the resistance is denoted $M_{c,Rd}$, and for the two Tees section, denoted $M_{o,Rd}$, as given by Equations (1) and (2), respectively. For Class 1 or 2 cross-sections, the bending resistance is taken as the plastic moment resistance, $M_{pl,Rd}$ for solid sections and $M_{o,pl,Rd}$ for sections at openings. When different steel grades are used for the flanges and the web, the plastic moment is calculated using a combined approach, in which the contributions from the flange and web are proportional to their respective yield stresses [32]. For cross-sections under combined bending and shear, the plastic moment resistance should consider a reduced yield strength applied to the web's shear area if the design shear force exceeds 50 % of the section's plastic shear resistance [13,31].

$$\frac{M_{Ed}}{M_{c,Rd}} \leq 1 \tag{1}$$

$$\frac{M_{Ed}}{M_{o,Rd}} \leq 1 \tag{2}$$

According to EN 1993-1-13, for closely spaced openings where the web-post width (w) is smaller than the opening diameter (a_0), the resistance to web-post buckling is checked using Equation (3). This equation compares the design web-post buckling resistance, $N_{wp,Rd}$, with the compressive force acting on the web-post, $N_{wp,Ed}$, which is taken as the horizontal shear force acting on the web-post $(V_{wp,Ed})$.

$$\frac{N_{wp,Ed}}{N_{wp,Rd}} \leq 1 \tag{3}$$

The web-post buckling resistance is calculated using Equation (4), which considers the web-post cross-section area, the steel yield strength (f_y), the reduction factor (χ_{wp}), and the partial safety factor for stability, taken as $\gamma_{M1} = 1.00$. The value of χ_{wp} is obtained from buckling curve a of EN 1993-1-1 [31] and is a function of the relative slenderness of the web-post, $\bar{\lambda}_{wp}$. This relative slenderness is given by the expression $\bar{\lambda}_{wp} = \left(1.75\sqrt{w^2 + {a_0}^2}/t_w\right)/\lambda_1$, where λ_1 is the reference slenderness defined in EN 1993-1-1 [31].

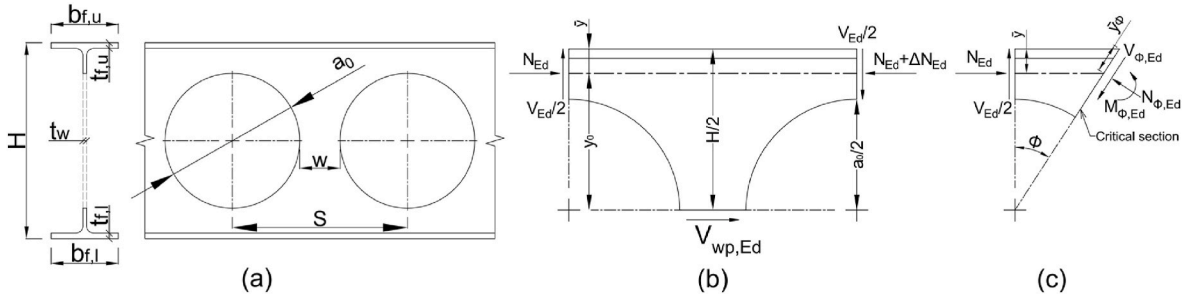

Fig. 1. Geometric parameters of a cellular beam; (b) Equilibrium of internal forces for the derivation of the horizontal shear force $(V_{wp,Ed})$; (c) Inclined cross-section for the Vierendeel mechanism.

$$N_{wp,Rd} = \chi_{wp} w t_w f_y \Big/ \gamma_{M1} \tag{4}$$

The horizontal shear force, $V_{wp,Ed}$, given by Equation (5), is derived from the equilibrium of internal forces acting on the beam [5], a principle that is illustrated schematically in Fig. 1(b). Its calculation involves the global vertical shear force, V_{Ed}, the spacing between the openings, S, and the distance $y_0 = H/2 - \bar{y}$, where $\bar{y}$ is the distance from the outer edge of the flange to the centroid of the Tee section.

$$N_{wp,Ed} = V_{wp,Ed} = V_{Ed} S \Big/ 2y_0 \tag{5}$$

Additionally, the resistance of the web-post to shear (WPS) must be verified. The horizontal shear force in the web-post should satisfy the condition given in Equation (6), where $V_{wp,Rd}$ is the design shear resistance of the web-post. This resistance is calculated by Equation (7), which considers the partial safety factor for resistance of cross-sections, taken as $\gamma_{M0} = 1.00$.

$$\frac{V_{wp,Ed}}{V_{wp,Rd}} \leq 1 \tag{6}$$

$$V_{wp,Rd} = w t_w f_y \Big/ \left(\sqrt{3}\,\gamma_{M0}\right) \tag{7}$$

EN 1993-1-13 also presents an alternative method for the Vierendeel bending verification, which consists of evaluating multiple inclined cross-sections around the web opening, as illustrated in Fig. 1(c). This verification is carried out on both sides of the opening. For each inclined section at an angle ϕ, from $-\phi_{max}$ to $+\phi_{max}$, where $\phi_{max} = \arctan(S/H)$, the resistance is evaluated by the interaction criteria given in Equation (8).

$$\frac{N_{\phi,Ed}}{N_{\phi,Rd}} + \frac{M_{\phi,Ed}}{M_{\phi,Rd}} \leq 1 \tag{8}$$

The design axial resistance, $N_{\phi,Rd}$, is obtained from the cross-section compression resistance principles in Ref. [31], while the design moment resistance, $M_{\phi,Rd}$, is determined analogously to the plastic bending resistance of a Tee section, assuming no axial force, as described in Ref. [2]. Both resistances are calculated from the geometry of the Tee section as projected onto the inclined plane. The axial force $N_{\phi,Ed}$ and the bending moment $M_{\phi,Ed}$ are derived from the equilibrium of forces acting on the beam [10]. On the high moment side of the opening, these design actions are calculated using Equations (9) and (10). The calculation of $M_{\phi,Ed}$ requires the position of the centroid of the inclined Tee section, $\bar{y}_\phi$, illustrated in Fig. 1(c).

$$N_{\phi,Ed} = N_{Ed} \cos\phi - (V_{Ed}/2)\sin\phi \tag{9}$$

$$M_{\phi,Ed} = (V_{Ed}/2)\left(H \Big/ 2 - \bar{y}_\phi \cos\phi\right)\tan\phi + N_{Ed}\left(\bar{y}_\phi \cos\phi - \bar{y}\right) \tag{10}$$

In the absence of a specific standard for fire design, the same verification equations applied to cellular beams at ambient temperatures are used for beams at elevated temperatures. However, the material reduction factors follow the values from EN 1993-1-2 [14], as recommended at the annex E, calculated from the experimental average temperatures using linear interpolation. For all calculations at elevated temperatures, the partial safety factor for resistance was taken as $\gamma_{M,fi} = 1.0$. In addition, for the calculation of the resistance to web-post buckling, the reduction factor for flexural buckling in fire design, χ_{fi}, as defined in Ref. [14], is considered.

3. Experimental tests

Experimental tests were conducted on both solid and cellular beams, with variations in geometric parameters and test temperatures. The cellular beams were fabricated from a parent IPE 220 I-beam (nominal dimensions: height = 220 mm, flange width = 110 mm, web thickness = 5.9 mm, and flange thickness = 9.2 mm), made of S275 steel. In each test, the beams were simply supported, with a load applied at mid-span. Vertical displacements were measured in all tests, while the strain behaviour was only measured during the ambient temperature tests. For the fire condition tests, the temperature was increased using an electro-ceramic resistance heating system. Once the beams reached the test temperature under steady-state conditions, the load was applied until failure.

3.1. Test specimens

The experimental sample set consisted of six cellular beams (B1, B2_1, B2_2, B2_3, B2_4, and B3) and one solid beam (B4). Beams B1, B2_1, B3, and B4 were tested at ambient temperature, while beams B2_2, B2_3, and B2_4 were tested at elevated temperatures of 500 °C, 600 °C, and 700 °C, respectively, as the usual critical temperature design values are withing this range. The beams tested at ambient temperature were fabricated with different opening diameters and spacings between the openings. In contrast, the four B2 beams were made with identical geometric parameters to specifically analyse the influence of temperature on collapse modes. Fig. 2 illustrates the experimental beam designs, with the dimensions of these key geometric parameters, along with the web-post width defined by $w = S - a_0$. All beams had an unrestrained length (L) of 3 m, with no openings in the mid-span region. Beam B1 had the smallest opening diameter and 10 openings, while the other beams each had 8 openings. To prevent failure near the supports, the last openings of beams B1 and B3, as well as the last two openings of the B2 series beams, were filled. Circular steel plates, fabricated from the same material as the parent web, were produced by welding two semi-circular halves with a central vertical butt weld. Each plate was then inserted into the opening and secured to the web with a continuous fillet weld along its perimeter, thus restoring a solid web section at these critical locations. All welds were done by electric arc welding using MAG process. Additionally, vertical welded stiffeners, made from the web material, were added at both support locations and at mid-span, where the load was applied.

Before testing, the geometric dimensions and lateral imperfections of each specimen were measured at various sections along the beams, with the corresponding averages presented in Table 1. The height of the beams is denoted by H, while the parameters $b_{f,u}$ and $b_{f,l}$ represent the widths of the upper and lower flanges, respectively. The web thickness is denoted by t_w , with $t_{f,u}$ and $t_{f,l}$ referring to the thicknesses of the upper and lower flanges. The remaining notations presented in Table 1 are provided in Fig. 2. The maximum amplitudes of the lateral geometric imperfections (δ_{max}) were measured using a laser aligned longitudinally parallel to the beam. Measurements were taken at 300 mm intervals along the length of the beam, on both the upper and lower flanges as well as the web. These manufacturing tolerances comply with the essential tolerances of the EN 1090–2:2018 [33], regarding welded sections manufactured from split rolled sections, namely the cellular beams overall section depth (H) and web geometry.

A material characterization study was conducted at ambient temperature on an IPE 220 profile to determine its primary mechanical properties. Three machined specimens were extracted from the flange and six from the web, prepared in accordance with EN ISO 377 [34]. Tensile tests were carried out following EN 10002-1 [35], using an Instron 4485 universal testing machine with a maximum capacity of 200 kN. A mechanical extensometer with a gauge length of 50 mm was used to accurately measure strains during the tests. Table 2 presents the tensile test results, including the yield strength (f_y), ultimate stress (f_u), and modulus of elasticity (E). The results indicate that the flange exhibited higher yield strength and ultimate tensile strength compared to the web, aligning with trends reported in previous studies [20,36]. The average modulus of elasticity determined from all tests was ≈200 GPa.

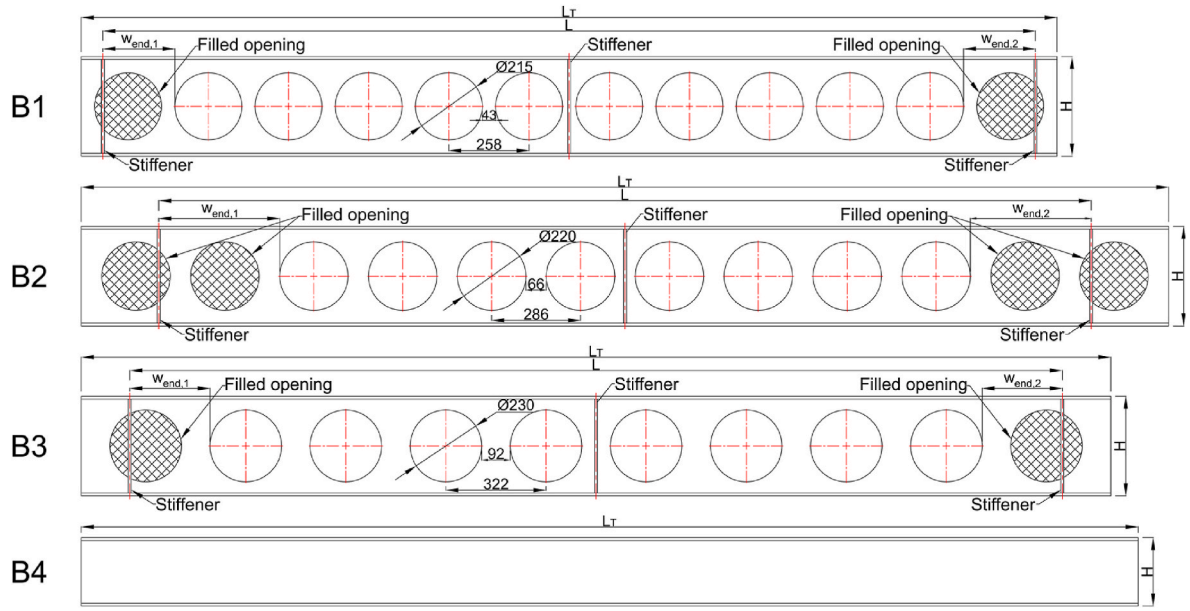

Fig. 2. Desing of experimental beams.

Table 1
Averages measured dimensions of specimens (all values in mm).

Specimen	H	$b_{f.u}$	$b_{f.l}$	$t_{f.u}$	$t_{f.l}$	t_w	a_0	S	$w_{end.1}$	$w_{end.2}$	L	L_T	δ_{max}
B1	321.0	110.9	110.2	8.9	9.0	6.5	215	258	230.0	231.5	2998.0	3140.0	2.5
B2_1	323.2	110.8	111.9	9.3	9.0	6.3	220	286	388.0	388.0	2998.0	3488.0	2.0
B2_2 (T = 500 °C)	323.0	111.4	111.0	8.9	9.1	6.4	220	286	387.5	386.7	2996.2	3488.2	2.0
B2_3 (T = 600 °C)	319.8	114.0	112.7	8.4	8.7	6.3	220	286	389.0	389.0	3000.0	3494.0	2.5
B2_4 (T = 700 °C)	321.5	110.9	110.3	9.1	9.3	6.5	220	286	389.0	389.0	3000.0	3489.0	2.5
B3	321.8	110.3	110.3	9.1	9.3	6.5	230	322	257.0	257.0	2998.0	3304.0	2.0
B4	219.8	111.0	110.3	9.0	9.3	6.4	–	–	–	–	3000.0	3396.0	0.5

Table 2
Tensile test results.

Flange test piece	$f_{y.f}$ [Mpa]	f_u [Mpa]	E [GPa]	Web test piece	$f_{y.w}$ [Mpa]	f_u [Mpa]	E [GPa]
$P_{f,1}$	387.79	507.99	204.94	$P_{w,1}$	315.66	433.84	208.96
$P_{f,2}$	386.97	506.93	190.20	$P_{w,2}$	321.53	432.61	201.33
$P_{f,3}$	395.66	508.77	182.17	$P_{w,3}$	312.89	433.07	207.27
Average	390.14	507.90	192.44	$P_{w,4}$	313.97	433.84	208.16
St. dev.	3.92	0.76	9.43	$P_{w,5}$	322.91	437.09	212.59
				$P_{w,6}$	320.75	433.38	204.72
				Average	317.95	433.97	207.17
				St. dev.	3.92	1.46	3.51

3.2. Experimental setup

The tests were conducted on a steel portal frame, with the complete experimental setup shown in in Figs. 3 and 4. The beams were supported at both ends by fork supports, and the load was applied at mid-span using a hydraulic actuator with an integrated load cell. Vertical displacements were measured using linear variable differential transducers (LVDTs), positioned on the lower flange: one at mid-span and two others at $L/4$ and $3L/4$ along the beam length. To prevent lateral-torsional buckling, four IPE 100 profiles were used as lateral restraints, in contact with both flanges on either side of the beam.

For tests at ambient temperature, strain gauges were attached to measure local strain within the elastic range, particularly around the two Tee section and web-post on the cellular beams, and in the mid-span section on the solid beam, as detailed in Fig. 5.

The high-temperature tests were conducted using an electro-ceramic heating system, with 19 electrical resistances (R_1 to R_{19}) connected to a Mannings heating system, model 16300, and distributed along the length of the beam. The beam was insulated by 50 mm thick ceramic mat. The tests were performed in the load domain, with the load applied until collapse, defined by a runaway vertical displacement, after the temperature had stabilized at a steady-state condition.

The methodology agrees with the EN 1363–1:2020, [37], performance criteria for flexural elements tested in fire conditions for which the load bearing capacity is based on the limiting deflection, given by $D_{limit} = L^2/400H$ and the limiting rate of deflection, defined by $(dD/dt)_{limit} = L^2/9000H$, resulting in $D_{limit} = 70.3$ mm and $(dD/dt)_{limit} = 3.13$ mm/min. Fig. 6 shows beam B2 with the electrical resistances in place, along with the 15 type K thermocouples (T_1 to T_{15}) with 0.711 mm wire diameter, distributed across 5 sections to monitor the beam's overall temperature. These thermocouples were attached directly to the

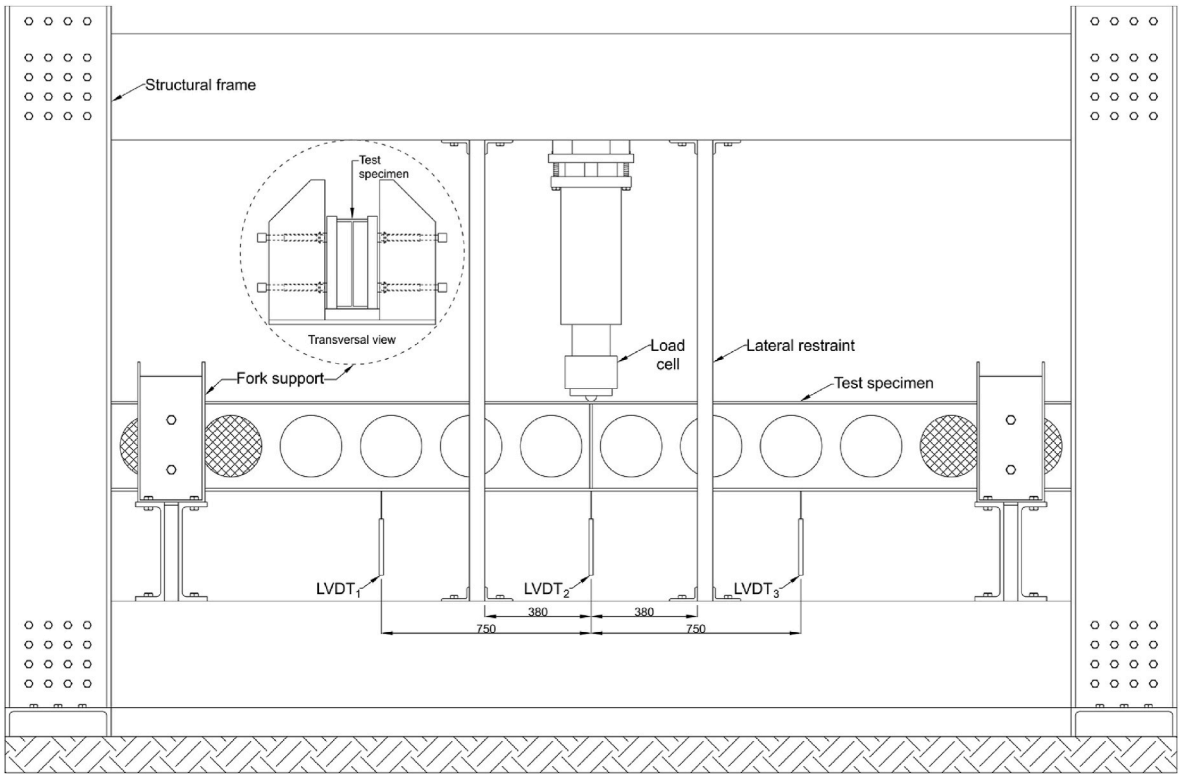

Fig. 3. Experimental test setup.

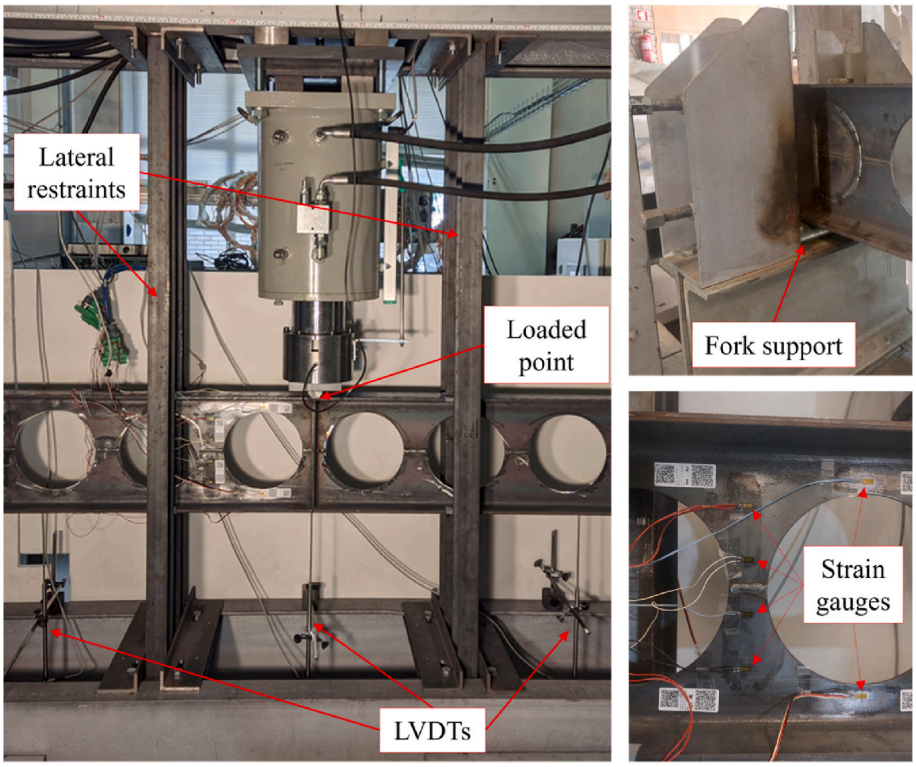

Fig. 4. Experimental test setup (photographic views).

steel surface by thermocouple welding, using a capacitor discharge spot welding machine.

4. Results and discussion

Table 3 presents a summary of the key experimental results, including the maximum applied load (F_{exp}) and the corresponding

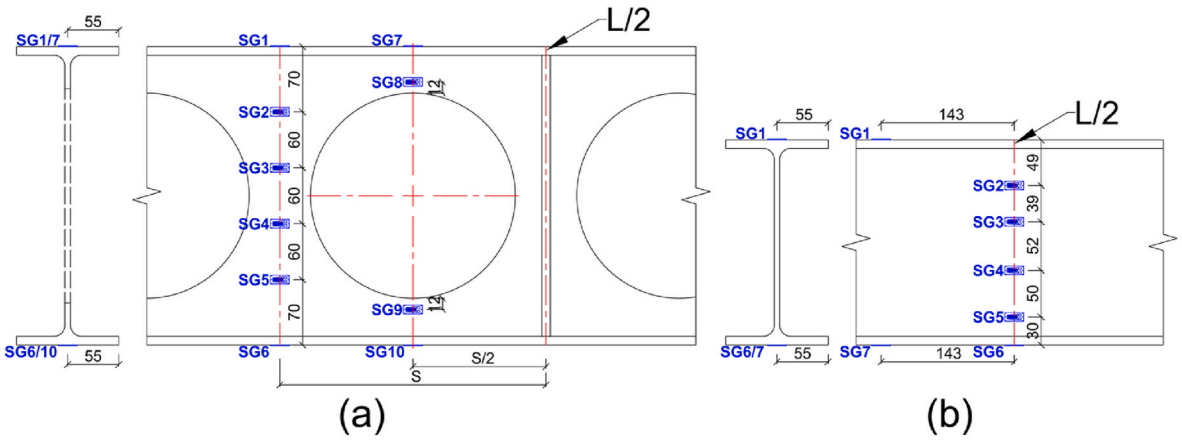

Fig. 5. Location of strain gages (SG) at: (a) cellular beams, (b) solid beam B4.

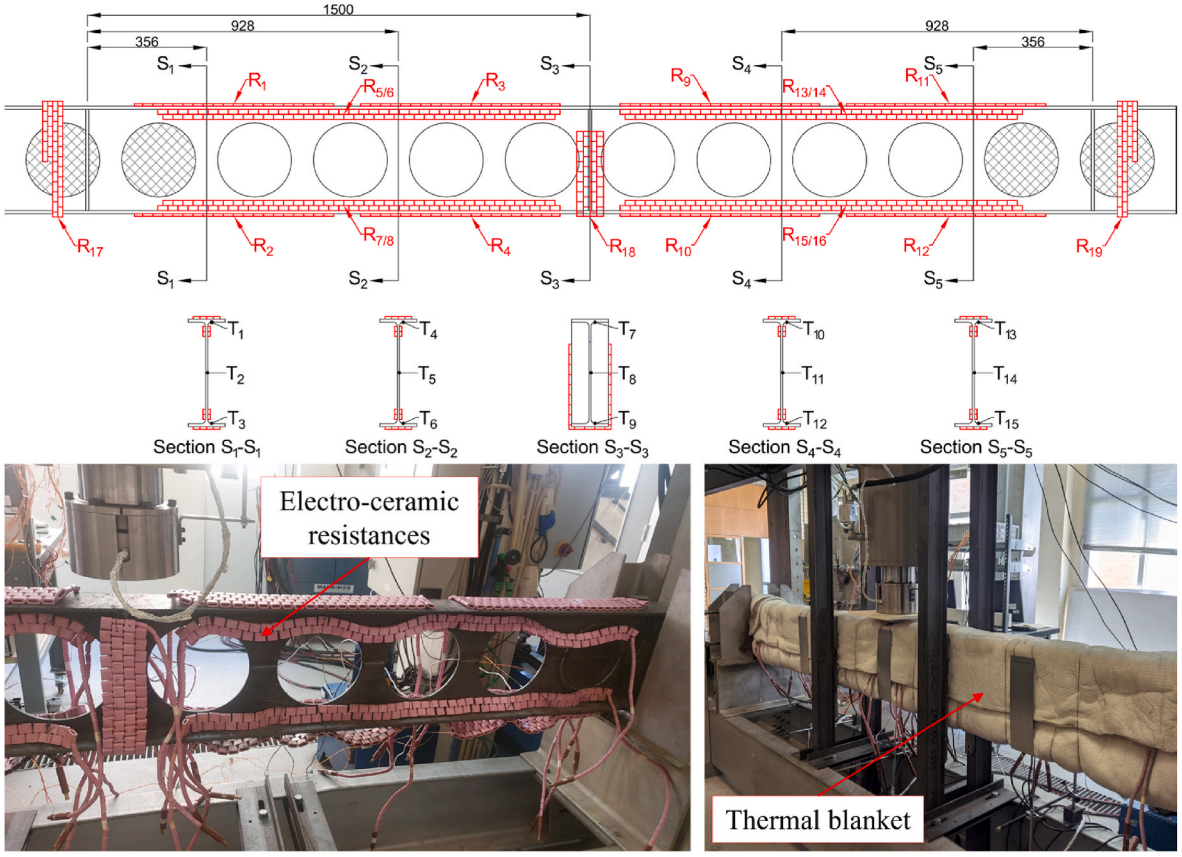

Fig. 6. Electro-ceramic resistances and thermocouples.

Table 3
Experimental tests results.

Specimen	F_{exp} [kN]	Displacement at F_{exp} [mm]			$M_{exp,MAX}$ [kN.m]	$M_{exp,2T}$ [kN.m]	$M_{pl,Rd}$ [kN.m]	$M_{o,pl,Rd}$ [kN.m]	Collapse mode
		$LVDT_1$	$LVDT_2$	$LVDT_3$					
B1	142.2	23.5	51.5	20.4	106.6	97.42	168.5	143.3	WPB
B2_1	174.1	14.3	33.5	12.3	130.5	118.05	171.4	139.2	WPB
B2_2 (T = 500 °C)	123.5	13.5	29.8	12.0	92.5	83.69	143.1	120.3	WPB
B2_3 (T = 600 °C)	75.4	17.3	36.6	13.7	56.5	51.13	86.6	72.4	WPB
B2_4 (T = 700 °C)	40.8	13.3	28.4	13.4	30.6	27.67	64.1	54.9	VM
B3	174.3	24.4	51.4	21.6	130.7	116.62	171.3	131.9	VM
B4	133.9	14.5	25.7	15.8	100.4	–	104.1	–	Plastic collapse

vertical displacements. This table details both the maximum experimental bending moment at mid-span $(M_{exp,MAX})$ and, for the cellular beams, the experimental moment at the perforated cross-section of the first opening adjacent to the mid-span $(M_{exp,2T})$. The analytical plastic moment capacities $M_{pl,Rd}$ and $M_{o,pl,Rd}$ are also given, allowing a direct comparison between the experimental behaviour and the theoretical capacity. For this calculation, the geometric asymmetry of the cross-section was simplified by using an equivalent symmetric profile, where the flange width and thickness were taken as the average of the measured upper and lower flange dimensions presented in Table 1. The experimental results are analysed in detail in the following sections, separated by tests performed at ambient and elevated temperatures.

It can be observed that only the solid beam B4 achieved an experimental moment close to its plastic moment resistance, confirming a global plastic collapse. The reason for this distinct behaviour is that, in the absence of web openings, the beam's load-bearing capacity is governed by the full yielding of its cross-section. In contrast, the cellular beams failed at a lower experimental moment due to the presence of the openings, which introduce specific local failure modes. These mechanisms, such as the WPS, WPB and Vierendeel mechanism observed in the cellular beams, are triggered before the entire cross-section can yield, thus preventing them from reaching their theoretical plastic moment resistance.

Based on the safety verifications recommended by EN 1993-1-13, detailed in Section 2, the design loads that would cause failure by each of the primary collapse modes were calculated. For the Vierendeel mechanism verification, the analysis was performed for the opening adjacent to the mid-span, representing the most critical section, with the minimum resistance consistently found at a critical angle of 25°. For this section the average temperature from the mid-span section S_3-S_3 (T_7, T_8 and T_9) was considered. Regarding the calculations for WPB and WPS the global average beam temperature (T_{avg}) was applied. Table 4 presents these design load values and compares them with the experimental results through the load ratios between the maximum experimental load (F_{Exp}) and the governing Eurocode design value (F_{EC3}). For the beams tested at elevated temperatures, the table also shows the ratio considering the standard deviation of the measured temperatures. These calculations provide a basis for comparing the experimental results discussed in Sections 4.1 and 4.2, which cover tests conducted at ambient and elevated temperatures, respectively.

4.1. Tests at ambient temperature

The load-displacement curves for the tests at ambient temperature are presented in Fig. 7. For beam B1, illustrated in Fig. 7(a), the mid-span vertical displacement ($LVDT_2$) was substantially larger than those measured at L/4 and 3L/4. The displacement recorded by $LVDT_3$ was smaller than that of $LVDT_1$, which is a result of the final failure occurring on the right side of the beam (see Fig. 8). The small peaks observed in the force-displacement curves in Fig. 7 are due to the increase in the actuator's displacement speed during the test. This adjustment was necessary to compensate for the reduction in load ap'lication resulting from the loss of beam stiffness.

Table 4
Comparison between experimental and Eurocode design values.

Specimen	F_{WPB} [kN]	F_{WPS} [kN]	F_{VM} [kN]	F_{EC3}	F_{exp}/F_{EC3}	
B1	171.8	120.1	127.8	120.1	1.18	
B2_1	223.8	162.9	126.2	126.2	1.38	
B2_2 (T = 500 °C)	125.8	139.3	103.0	103.0	1.20	+0.03 −0.03
B2_3 (T = 600 °C)	72.8	85.0	56.3	56.3	1.34	+0.23 −0.22
B2_4 (T = 700 °C)	51.9	61.7	38.8	38.8	1.05	+0.19 −0.14
B3	272.8	205.9	117.1	117.1	1.49	

Notes: F_{WPB} represents the calculated failure load for web-post buckling; F_{WPS} is the calculated failure load for web-post shear; and F_{VM} is the calculated failure load for the Vierendeel mechanism. F_{EC3} represents the design failure load according to Eurocode, taken as the minimum value from all failure modes (F_{EC3} = min (F_{WPB}, F_{WPS}, F_{VM})).

The failure mechanism of beam B1, which had the smallest opening diameter and spacing, was identified as web-post buckling. This conclusion is supported by the final deformed shape, shown in Fig. 8, clearly presents the characteristic S-shaped buckling of a web-post. Moreover, this instability-driven failure is corroborated by the strain gauge data presented in Fig. 9 (a). The strain gauges measured strain (ε) within the material's elastic range, with yield limits of ±1590 μm/m for the web and ±1951 μm/m for the flange. The curves show a distinct reversal in the strain direction at a load of approximately 100 kN, a classic behaviour of a buckling phenomenon, which aligns with the loss of strength observed in the load-displacement curve at the same point.

A comparison between the experimental results and the Eurocode predictions in Table 4 reveals a significant finding for this beam. The experimental ultimate load of 142.2 kN is positioned between the two primary web-post resistances predicted by the code. The experimental failure load surpassed the predicted WPS resistance (F_{WPS}) of 120.1 kN by approximately 18 %, suggesting that the Eurocode's design model for WPS was conservative for this specimen. Conversely, the beam failed before reaching its predicted WPB resistance (F_{WPB}) of 171.8 kN, with the experimental load being 17 % lower, which indicates that the design model for WPB was non-conservative in this case.

This difference suggests that the Eurocode's approach of treating these failure modes as independent phenomena could not fully capture the complex interaction between them. A more plausible explanation is that the high shear stress state in the web-post, as the load surpassed the theoretical WPS limit, induced partial plastic yielding. This shear-induced yielding likely reduced the effective stiffness of the web-post, thereby precipitating the observed instability failure (WPB) at a load lower than the theoretical resistance calculated for a fully elastic section.

As shown in Fig. 8, beam B2_1 also exhibited a failure characterized by WPB, with the local instability observed on the right side of the beam. It failed at a maximum experimental load of 174.1 kN. The load-displacement curves in Fig. 7(b) indicate that B2_1 had the smallest vertical displacement among the cellular beams tested at ambient temperature, reaching a maximum of 33.5 mm at mid-span. Shortly after reaching its peak load, $LVDT_1$ lost contact, ending its data recording. The strain gauges in the web provided further insight into the failure mechanism; as shown in Fig. 9 (b), they displayed a loss of linearity and a distinct reversal in strain near a load of 145 kN, confirming the onset of local instability consistent with a WPB failure.

However, a comparison with the Eurocode predictions from Table 4 reveals a notable discrepancy between the predicted and observed behaviour. Contrary to the experimental WPB failure, the Eurocode's governing failure mode prediction was for the Vierendeel mechanism, with a design resistance (F_{EC3}= F_{VM}) of only 126.2 kN. This prediction proved to be highly conservative, as the experimental ultimate load of 174.1 kN surpassed it by 38 %. Furthermore, the design model for WPS was also found to be conservative, with the experimental load exceeding the predicted resistance (F_{WPS} = 162.9 kN) by 7 %. In contrast, and consistent with the findings for beam B1, the model for the observed WPB failure mode proved to be non-conservative, as the collapse occurred at a load 22 % lower than the theoretical resistance (F_{WPB} = 223.8 kN).

This highlights the limitations of the simplified design models in capturing the true failure mode for this geometry under three-point bending. The high shear forces inherent to the test setup likely promoted a shear-driven instability (WPB) over a bending-driven one (VM), even though the latter had a lower theoretical resistance. The interaction mechanism, where high shear stresses induced yielding that precipitated

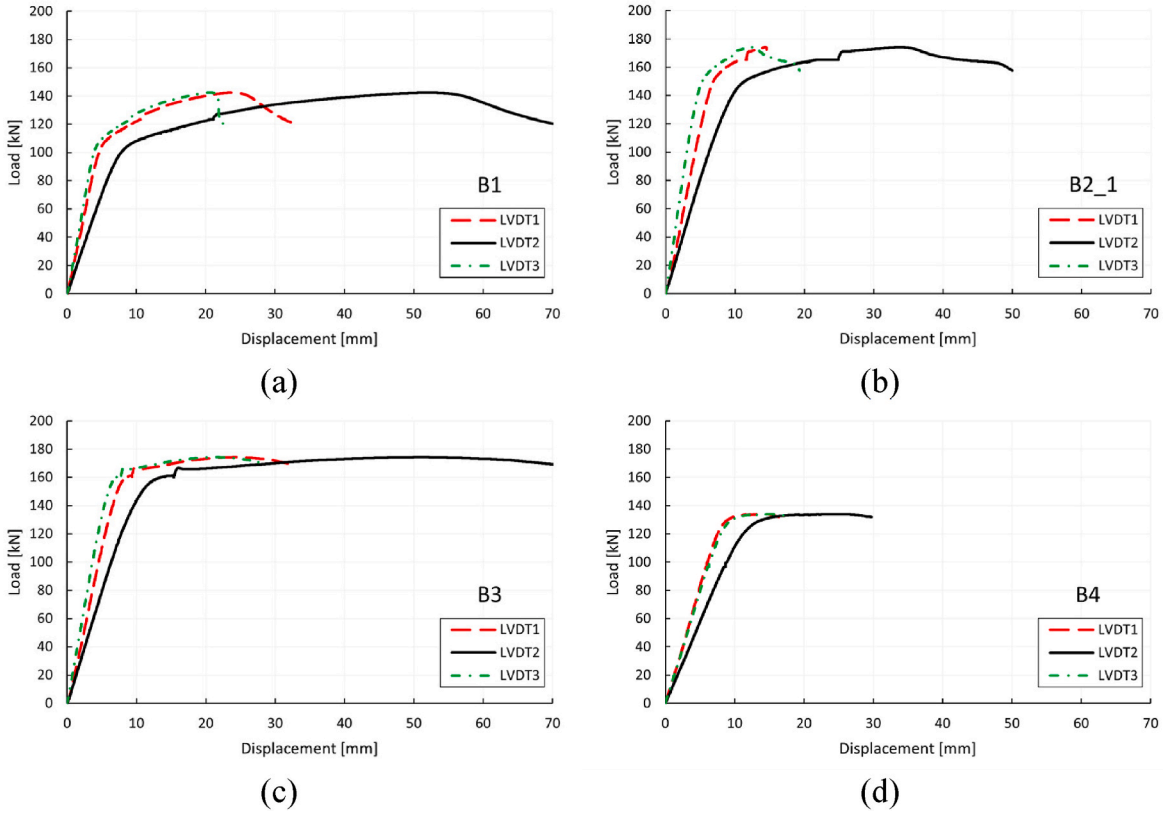

Fig. 7. Load-displacement behaviour of tests at ambient temperature.

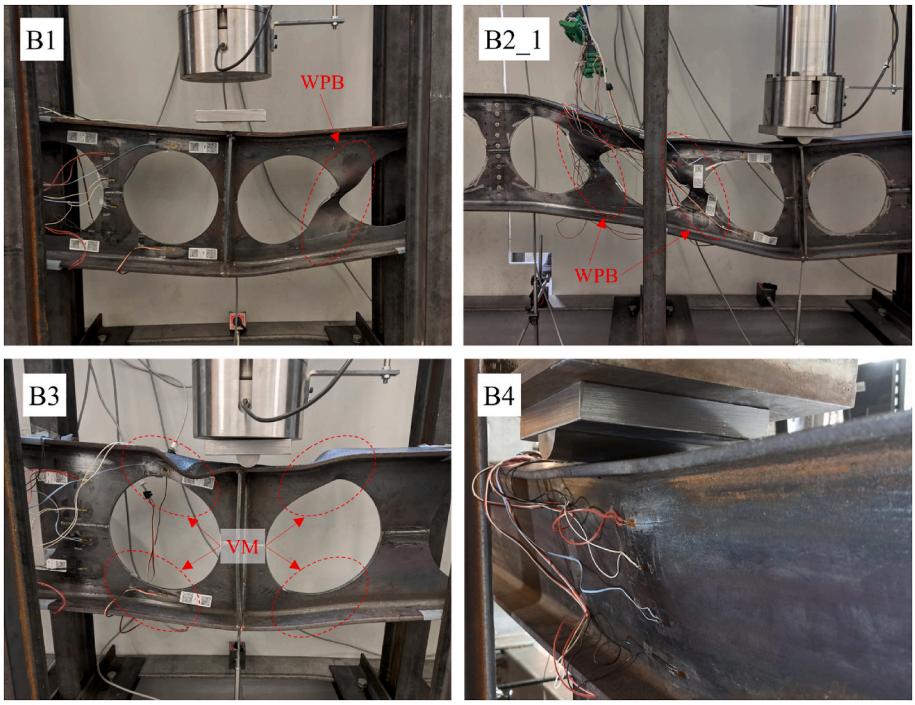

Fig. 8. Specimen failures modes of tests at ambient temperatures.

a premature WPB failure, remains the most plausible explanation for the observed collapse.

Although both beams B1 and B2_1 ultimately failed by WPB, the experimental load capacity of beam B2_1 (174.1 kN) was significantly higher than that of beam B1 (142.2 kN). This difference is explained by the web-post geometry. The larger opening spacing in B2_1 created a wider web-post ($w = 66$ mm) compared to that of B1 ($w = 43$ mm). This wider web-post provides a larger cross-sectional area and a lower slenderness ratio, which increases its resistance to both shear and buckling. This is directly reflected in the analytical predictions presented in

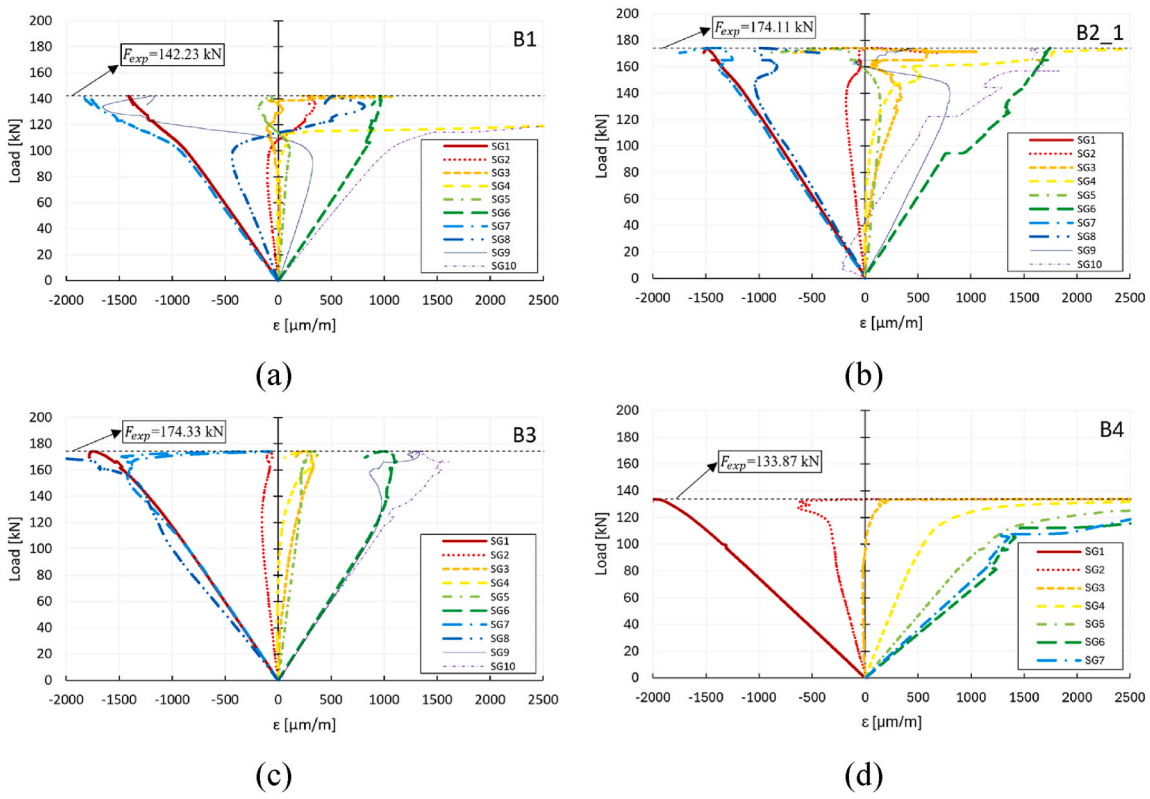

Fig. 9. Load-strain behaviour of tests at ambient temperature.

Table 4, where the calculated resistances F_{WPS} and F_{WPB} for B2_1 are notably higher than for B1.

Unlike the other cellular beams that failed due to WPB, specimen B3 failed by the Vierendeel mechanism. This was evidenced by the formation of plastic hinges in the Tees around the two central openings, as shown in Fig. 8. The maximum experimental load reached 174.3 kN, corresponding to a mid-span displacement of 51.4 mm. The load-strain curves in Fig. 9 (c) support this failure mode assessment; in contrast to beams B1 and B2_1, they do not exhibit the significant strain reversal associated with buckling. The Eurocode predictions in Table 4 correctly identify the VM as the governing failure mode, but the calculated design resistance (F_{EC3}= F_{VM}) of 117.1 kN is significantly lower than the experimental result. The beam's actual capacity surpassed this prediction by approximately 49 %, indicating that the Eurocode's design model for the Vierendeel mechanism was highly conservative for this specimen.

Beam B4, the solid reference beam, reached its full plastic moment capacity, with the cross-section yielding across its entire depth, as shown in Fig. 8. This plastic collapse occurred at a maximum applied load of 133.9 kN and a mid-span displacement of 25.7 mm. Fig. 9(d) illustrates that the load-strain curves for almost all strain gauges exhibited a loss of linearity at approximately 115 kN, consistent with the load-displacement behaviour observed in Fig. 7(d). The formation of a plastic hinge was clearly confirmed by the strain gauges, as they showed that strain continued to increase significantly even after the load had stabilized. This global collapse mechanism also explains why the solid beam B4 showed significantly less displacement at its maximum load, which is attributed to its high shear stiffness and failure governed by a plastic hinge, in contrast to the more flexible, local failure mechanisms observed in the cellular beams that allow for larger deformations.

4.2. Tests at elevated temperature

The temperature of the beams was monitored using thermocouples throughout all the experimental tests. Fig. 10(a) shows the evolution of the average temperature for each beam, including standard deviation bars, at the initial instant of the loading process. Additionally, Table 5 provides the temperatures recorded by all thermocouples at the beginning of load application, with global average values (T_{avg}) of 471 °C, 581 °C, and 640 °C for beams B2_2, B2_3, and B2_4, respectively. Beam B2_4 exhibited the highest standard deviation, which can be attributed to its exposure to the highest temperature. Although the beam was thermally insulated, heat loss still occurred at the ends. The end sections, S_1- S_1 and S_5- S_5 (see Fig. 6) exhibited lower temperatures compared to the other monitored sections.

It is important to note that, throughout the test, the beam was covered by a thermal ceramic blanket, preventing observation of its deformation during load application. Consequently, Fig. 11 presents the beam's configurations after load removal and subsequent cooling, highlighting the presumed failure mode based on its final configuration.

As shown in Fig. 10(b) and (c), beams B2_2 (at 471 °C) and B2_3 (at 581 °C) failed at maximum experimental loads of 123.5 kN and 75.4 kN, respectively. In both cases, the observed failure mode was web-post buckling, as indicated by their final deformed shapes in Fig. 11. The theoretical WPB resistance (F_{WPB}) provided an excellent prediction of the actual failure load for both beams, with load ratios of 0.98 and 1.04 for B2_2 and B2_3, respectively. However, the minimum load value comes from the Vierendeel mechanism (F_{EC3}= F_{VM}) showing that Eurocode do not predict correctly the collapse mode for these two beams. This governing VM prediction proved to be conservative in both tests, with the experimental load surpassing the prediction by 20 % for B2_2 and 34 % for B2_3.

The specific location of the WPB failure was also analysed. For beam B2_2, the failure on the left side correlates directly with the measured temperature distribution, as the web on this side was hotter (T_5 = 460 °C) than on the right side (T_{11} = 445 °C), thus making it more susceptible to instability. In the case of beam B2_3, however, the failure occurred on the cooler right side (T_{11} = 542 °C), even though the left

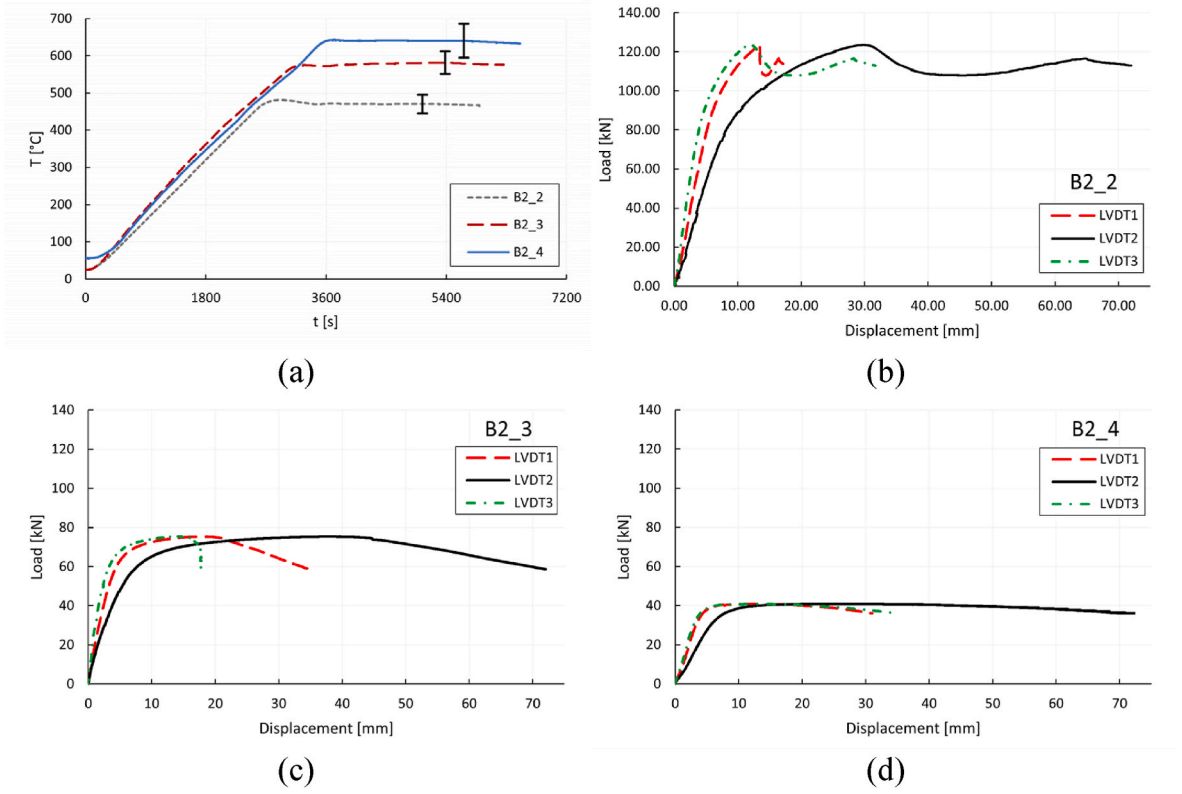

Fig. 10. Average temperatures and load-displacement behaviour of tests at elevated temperatures.

Table 5
Temperature at beginning of load application.

Specimen	T [C]															T_{avg}	St. dev.
	Section S_1-S_1			Section S_2-S_2			Section S_3-S_3			Section S_4-S_4			Section S_5-S_5				
	UF	W	LF	UF	W	LF	UF	W	LF	UF	W	LF	UF	W	LF		
	T_1	T_2	T_3	T_4	T_5	T_6	T_7	T_8	T_9	T_{10}	T_{11}	T_{12}	T_{13}	T_{14}	T_{15}		
B2_2	459	434	471	455	460	502	469	485	490	474	445	512	489	419	502	471	25
B2_3	601	531	585	594	565	612	560	605	631	579	542	603	595	520	594	581	30
B2_4	644	538	671	649	589	711	641	671	690	636	605	697	645	572	647	640	46

Notes: UF = Upper Flange; W = Web; LF = Lower Flange.

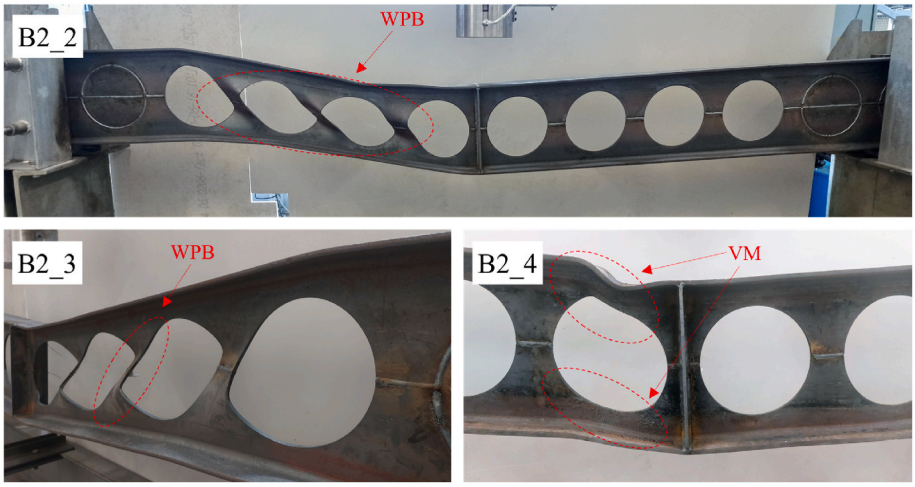

Fig. 11. Specimen failures modes of tests at elevated temperatures.

side was significantly hotter ($T_5 = 565$ °C). This apparent contradiction suggests that the failure location was governed by a complex interaction of factors beyond the thermal gradient, such as the initial geometric imperfection (which had a maximum amplitude of $\delta_{max} = 2.5$ mm for this beam), alongside minor local variations in steel strength (material inhomogeneity) and the presence of residual stresses from the cutting and welding process. Together, this combination of effects could have governed the onset of instability on the right side.

In contrast to the other specimens, beam B2_4, tested at the highest average temperature of 640 °C, failed due to the Vierendeel mechanism, as shown in Fig. 11. This local deformation occurred locally in the left-hand central opening. Its maximum experimental load was 40.8 kN, with a corresponding mid-span displacement of 28.4 mm. The load-displacement behaviour of beam B2_4, shown in Fig. 10(d), closely resembles that of beam B3 in Fig. 9(c), which also failed due to VM. In this case, the Eurocode prediction in Table 4 correctly identified the VM as the governing failure mode ($F_{EC3} = F_{VM} = 38.8$ kN), with an experimental failure load of 40.8 kN, resulting in a load ratio equal to 1.05.

The asymmetric failure of beam B2_4 highlights the influence of the thermal conditions along its length. Temperature data in Table 5 show that the left-hand side, where the Vierendeel mechanism occurred, was subjected to the most severe thermal exposure. At section S_2-S_2, a significant cross-sectional gradient of 122 °C was measured between the hotter upper flange (711 °C) and the cooler web (589 °C), whereas the corresponding gradient on the right side (S_4-S_4) was lower, of 92 °C. The average temperature at S_2-S_2 (683 °C) was also higher than at S_4-S_4 (646 °C), indicating that the left side of the beam was comparatively weaker. These localized thermal conditions can be considered as the main factor governing the left-side collapse, leading to the Vierendeel mechanism as the predominant failure mode.

The analysis of the beams at elevated temperatures highlights some limitations in the current Eurocode approach. The code's method of selecting the minimum resistance from independent failure modes failed to predict the correct collapse mechanism for the beams at 500 °C and 600 °C, which failed by WPB despite VM being the expected mode. Furthermore, an analysis of the load ratios in Table 4, which considers the standard deviation from the cross-section temperature variation, shows that the code's predictions are still safe when the smaller temperatures at the sections are used. For the tests at 500 °C and 600 °C, the conclusion that the Eurocode's governing prediction is conservative holds true across the entire uncertainty range, within the standard deviation interval. For the test at 700 °C, the load ratio of 1.05 suggests a conservative prediction, but the uncertainty analysis in Table 4 shows a possible unsafe margin, considering the temperature variation in the section, with a load ratio variation equal to −0.14 and + 0.19.

This suggests that the simple application of material reduction factors to ambient temperature equations may not adequately capture the complex behaviour of cellular beams in fire, where thermal gradients and the interaction between failure modes become more relevant, and the need for additional formulae to account for the efforts interaction in the Vierendeel mechanism safety verification. As noted in previous works, particularly for the shear buckling strength of web-posts of castellated steel beams [12], and the collapse mechanics of web post buckling and Vierendeel bending [38], while design formulations for ambient temperature show acceptable agreement, these results confirm that additional refinements are needed for elevated temperature design. Additionally, regarding the Vierendeel load underestimation, when using the linear interaction curve, can be corrected by using a nonlinear relation of the axial and bending efforts, and including the shear effect [10,39].

5. Conclusions

Motivated by a lack of experimental research in the steady-state and the inexistence of specific design rules for fire conditions, the behaviour of cellular beams under three-point bending were studied experimentally, allowing to obtain the loadbearing capacity at ambient temperature and constant and identifying the collapse modes.

A total of seven specimens were loaded until failure. Three cellular beams at ambient temperature, three at elevated temperatures, cut from an IPE 220 (S275), and one additional solid beam as a reference and setup calibration. Opening ratios (a_0/h) from 0.98 to 1.05, and spacing ratios (S/a_0) ranging 1.2 and 1.4 were used in the tested beams, considering constant beam length and section hight. End openings were selectively filled and vertical stiffeners placed at supports and under the load to avoid local failures. All beams had an unrestrained length of 3 m with no mid-span openings. During tests the temperature distribution, strains and vertical displacements were measured allowing to determine the collapse load.

The main conclusions can be summarized as follows:

At ambient temperature, the cellular beams exhibited local mechanisms governed by the web openings. Beams B1 and B2_1 failed by web-post buckling (WPB), with experimental maximum loads of 142.2 kN and 174.1 kN, respectively. Strain reversal data and S-shaped web-post deformation confirmed instability, and the higher capacity of B2_1 was consistent with its wider, less slender web-post. On the other hand, B3 failed by the Vierendeel mechanism (VM) with a plastic hinge formation in the Tees and with a maximum load of 174.3 kN.

Under elevated temperatures, the governing mode depended on both temperatures being also the resistance variable with the cross-section temperature variation. Beams B2_2 (T_avg ∼ 471 °C) and B2_3 (≈581 °C) failed by WPB at 123.5 kN and 75.4 kN, respectively, whereas B2_4 (≈640 °C) failed by VM at 40.8 kN.

Comparison with Eurocode design checks (EN 1993-1-13 at ambient, EN 1993-1-2 reductions at elevated temperature) showed that it is generally conservative to take the minimum of resistances, giving load ratios (F_{exp}/F_{EC3}) between 1.05 and 1.49, yet unreliable in identifying the collapse mode prediction. At ambient, Eurocode predicted VM collapse mechanism where tests failed by WPB (e.g., B2_1: VM design 126.2 kN vs. test 174.1 kN), while the WPB model itself proved to be non-conservative (e.g., B1: WPB design 171.8 kN vs. test 142.2 kN.

At elevated temperature, design calculations were conservative at ∼500–600 °C ($F_{exp}/F_{EC3} \approx 1.20$–$1.34$) but only marginal at ∼700 °C (≈1.05) and potentially unsafe when the cross-section temperature variability is considered. These results support the existence of interaction based on axial–bending–shear coupling in VM checks, as already pointed in Ref. [39], and a better fit using nonlinear relations [10,39].

Following the paper conclusions additional attention should be given to different failure modes of cellular beams and their interaction at elevated temperatures. For example, ultimate limit states like WPB and WPS main not originate collapse due to additional tension and compression resistance of the bottom and top T sections, leading to catenary action, as already considered by Zhang and Wang [40]. Other geometry properties and stiffnesses should be studied by using detailed and calibrated finite elements models.

CRediT authorship contribution statement

Luana V. da Silva: Writing – review & editing, Writing – original draft, Methodology, Investigation, Conceptualization. **Nickolas Giacomitti:** Investigation, Writing – original draft. **Débora Ferreira:** Supervision, Writing – original draft. **Nuno Lopes:** Supervision, Writing – original draft. **Luís M.R. Mesquita:** Writing – review & editing, Writing – original draft, Supervision, Methodology, Investigation, Conceptualization.

Declaration of competing interest

The authors declare that they have no known competing financial interests or personal relationships that could have appeared to influence the work reported in this paper.

Data availability

Data will be made available on request.

References

[1] S.S. Fares, J. Coulson, D.W. Dinehart, Steel Design Guide 31: Castellated and Cellular Beam Design, American Institute of Steel Construction, 2016.

[2] R.M. Lawson, S.J. Hicks, Design of composite beams with large web openings, in: Accordance with Eurocodes and the UK National Annexes, P355 ed., SCI, 2011.

[3] L.V. da Silva, L.M.R. Mesquita, Elastic lateral-torsional buckling of cellular beams, Structures 63 (2024) 106392, https://doi.org/10.1016/j.istruc.2024.106392.

[4] M.E.A. Ben Seghier, N. Elshaboury, E.M. Abdelkader, H. Carvalho, C.C. de Faria, L. F. Miguel, Two-stage framework for lateral-torsional buckling resistance prediction of cellular steel beams under fire conditions, Structures 68 (2024) 107157, https://doi.org/10.1016/J.ISTRUC.2024.107157.

[5] L.F. Grilo, R.H. Fakury, A.L.R. de Castro e Silva, G. de S. Veríssimo, Design procedure for the web-post buckling of steel cellular beams, J. Constr. Steel Res. 148 (2018) 525–541, https://doi.org/10.1016/J.JCSR.2018.06.020.

[6] V. Limbachiya, R. Shamass, Application of artificial neural networks for web-post shear resistance of cellular steel beams, Thin-Walled Struct. 161 (2021) 107414, https://doi.org/10.1016/J.TWS.2020.107414.

[7] R. Shamass, F.P.V. Ferreira, V. Limbachiya, L.F.P. Santos, K.D. Tsavdaridis, Web-post buckling prediction resistance of steel beams with elliptically-based web openings using Artificial Neural Networks (ANN), Thin-Walled Struct. 180 (2022) 109959, https://doi.org/10.1016/J.TWS.2022.109959.

[8] G. Promsatit, T. Sethaput, W. Atjanakul, A. Boonyaprapasorn, Enhancing web-post buckling resistance in perforated steel beams: an in-depth investigation of elliptical openings, geometric parameters, and ai-driven predictions, Structures 71 (2025) 107907, https://doi.org/10.1016/J.ISTRUC.2024.107907.

[9] H.J. Lee, Shear behavior of I-section steel with circular web opening and novel reinforcement, J. Constr. Steel Res. 201 (2023) 107637, https://doi.org/10.1016/J.JCSR.2022.107637.

[10] P. Panedpojaman, T. Thepchatri, S. Limkatanyu, Novel simplified equations for Vierendeel design of beams with (elongated) circular openings, J. Constr. Steel Res. 112 (2015) 10–21, https://doi.org/10.1016/J.JCSR.2015.04.007.

[11] B.M. Zeytinci, M. Şahin, M.A. Güler, K.D. Tsavdaridis, A practical design formulation for perforated beams with openings strengthened with ring type stiffeners subject to Vierendeel actions, J. Build. Eng. 43 (2021) 102915, https://doi.org/10.1016/J.JOBE.2021.102915.

[12] L.G.J. Miranda, J.C.L. Ribeiro, G. de S. Veríssimo, J.L.R. Paes, R.B. Caldas, Comparative analysis of fire-adapted models for the shear buckling strength of web-posts in castellated steel beams, Fire Saf. J. 138 (2023) 103796, https://doi.org/10.1016/J.FIRESAF.2023.103796.

[13] CEN, EN 1993-1-13, Design of Steel Structures - Part 1-13: Beams with Large Web Openings, 2024, 2024.

[14] CEN, EN 1993-1-2:2024, Design of Steel Structures - Part 1-2: General rules-structural Fire Design, 2024.

[15] V.K. Kotapati, A.P. Khatri, A new proposal for the design of laterally unrestrained cellular steel beams under moment gradient at elevated temperatures, Fire Saf. J. 140 (2023) 103812, https://doi.org/10.1016/J.FIRESAF.2023.103812.

[16] S.B. Oribi, A. Kada, B. Lamri, L. Mesquita, Behaviour of cellular steel beams at ambient and high-temperature conditions, J. Constr. Steel Res. 207 (2023) 107969, https://doi.org/10.1016/J.JCSR.2023.107969.

[17] L. Kang, S. Hong, X. Liu, Shear behaviour and strength design of cellular beams with circular or elongated openings, Thin-Walled Struct. 160 (2021) 107353, https://doi.org/10.1016/J.TWS.2020.107353.

[18] N. Boissonnade, J. Nseir, H. Somja, Experimental and numerical investigations towards the lateral torsional buckling of cellular steel beams, Thin-Walled Struct. 195 (2024) 111388, https://doi.org/10.1016/J.TWS.2023.111388.

[19] H. Amrous, N.M. Yossef, M.H. El-Boghdadi, Experimental study and structural analysis of tapered steel beams with cellular openings, Eng. Struct. 288 (2023) 116212, https://doi.org/10.1016/J.ENGSTRUCT.2023.116212.

[20] D. Sonck, J. Belis, Lateral–torsional buckling resistance of cellular beams, J. Constr. Steel Res. 105 (2015) 119–128, https://doi.org/10.1016/J.JCSR.2014.11.003.

[21] F. Erdal, M.P. Saka, Ultimate load carrying capacity of optimally designed steel cellular beams, J. Constr. Steel Res. 80 (2013) 355–368, https://doi.org/10.1016/J.JCSR.2012.10.007.

[22] K.D. Tsavdaridis, C. D'Mello, Web buckling study of the behaviour and strength of perforated steel beams with different novel web opening shapes, J. Constr. Steel Res. 67 (2011) 1605–1620, https://doi.org/10.1016/J.JCSR.2011.04.004.

[23] S.G. Morkhade, L.M. Gupta, An experimental and parametric study on steel beams with web openings, International Journal of Advanced Structural Engineering 7 (2015) 249–260, https://doi.org/10.1007/S40091-015-0095-4/FIGURES/20.

[24] B. Lamri, L. Mesquita, K. Abdelhak, P. Piloto, Behavior of cellular beams protected with intumescent coatings, Fire. Res. 1 (2016) 27, https://doi.org/10.4081/fire.2017.27.

[25] C. Bailey, Indicative fire tests to investigate the behaviour of cellular beams protected with intumescent coatings, Fire Saf. J. 39 (2004) 689–709, https://doi.org/10.1016/J.FIRESAF.2004.06.007.

[26] O. Vassart, C.G. Bailey, M. Hawes, A. Nadjai, W.I. Simms, B. Zhao, T. Gernay, J. M. Franssen, Large-scale fire test of unprotected cellular beam acting in membrane action, Proc. Inst. Civ. Eng.: Struct. Build. 165 (2012) 327–334, https://doi.org/10.1680/STBU.11.00019.

[27] K.A. Cashell, M. Malaska, M. Khan, M. Alanen, K. Mela, Experimental and numerical analysis of stainless steel cellular beams in fire, Fire Saf. J. 121 (2021) 103277, https://doi.org/10.1016/J.FIRESAF.2021.103277.

[28] E.H. Naili, A. Nadjai, S. Han, F. Ali, S. Choi, Experimental and numerical modelling of cellular beams with circular and elongated web openings at elevated temperatures, J. Struct. Fire Eng. 2 (2011) 289–300, https://doi.org/10.1260/2040-2317.2.4.289.

[29] P. Sunar Bükülmez, O.C. Celik, Experimental study on fire behavior of steel–concrete composite cellular beams with large opening ratio, Int. J. Steel Struct. 20 (2020) 207–231, https://doi.org/10.1007/S13296-019-00281-9/FIGURES/30.

[30] J. Claasen, R. Walls, A. Cicione, D. Streicher, Structural behaviour of a novel modular cellular steel beam system at elevated temperatures based on large-scale experimental testing and numerical modelling, J. Constr. Steel Res. 197 (2022) 107512, https://doi.org/10.1016/J.JCSR.2022.107512.

[31] CEN, EN 1993-1-1, Eurocode 3 - Design of Steel Structures - Part 1-1, General rules and rules for buildings, 2005.

[32] M. Veljkovic, B. Johansson, Design of hybrid steel girders, J. Constr. Steel Res. 60 (2004) 535–547, https://doi.org/10.1016/S0143-974X(03)00128-7.

[33] CEN, EN 1090-2:2018, Execution of Steel Structures and Aluminium Structures - Part 2: Technical Requirements for Steel Structures, 2018.

[34] CEN, EN ISO 377:1997, Steel and Steel Products - Location and Preparation of Samples and Test Pieces for Mechanical Testing, 1997.

[35] CEN, EN 10002-1:2001, Metallic Materials - Tensile Testing - Part 1: Method of Test at Ambient Temperature, 2001.

[36] S.G. Morkhade, L.M. Gupta, An experimental and parametric study on steel beams with web openings, International Journal of Advanced Structural Engineering 7 (2015) 249–260, https://doi.org/10.1007/s40091-015-0095-4.

[37] CEN, EN 1363-1:2020, Fire Resistance Tests - Part 1: General Requirements, 2020.

[38] A. Nadjai, E.H.A. Naili, S. Han, F. Ali, N. Goodfellow, S. Choi, Fire behaviour of cellular composite floor steel beams with different web opening shapes, Fire Saf. Sci. 10 (2011) 1537–1548, https://doi.org/10.3801/IAFSS.FSS.10-1537.

[39] P. Panedpojaman, W. Sae-Long, R. Yapa, P. Chaiviriyawong, Design of cellular members under axial-shear-flexure interaction, J. of App. and Comput. Mech. 10 (2024) 754–769, https://doi.org/10.22055/JACM.2024.45237.4335.

[40] L. Zhang, P. Wang, Simplified analysis method for catenary action of restrained cellular steel beams at elevated temperature considering strain reversal, Fire Saf. J. 95 (2018) 145–159, https://doi.org/10.1016/J.FIRESAF.2017.11.009.